MDPI

Article

Microstructure, Mechanical, Corrosion, and Ignition Properties of WE43 Alloy Prepared by Different Processes

Drahomír Dvorský [1,2,*] **, Jiří Kubásek** [1]**, Klára Hosová** [1]**, Miroslav Čavojský** [3] **and Dalibor Vojtěch** [1]

[1] University of Chemistry and Technology, Faculty of Chemical Technology, Department of Metals and Corrosion Engineering, Prague, Technická 5, 166 28 Prague 6, Czech Republic; kubasekj@vscht.cz (J.K.); klara.hosova@vscht.cz (K.H.); vojtechd@vscht.cz (D.V.)

[2] Institute of Physics, Czech Academy of Science, Prague, Na Slovance 1999/2, 182 21 Prague 8, Czech Republic

[3] Institute of Materials and Machine Mechanics SAS, Slovak Academy of Sciences, Dúbravská Cesta 9, 845 13 Bratislava, Slovakia; miroslav.cavojsky@savba.sk

* Correspondence: dvorsky@fzu.cz

Abstract: This paper deals with the effect of microstructure condition on ignition temperature, mechanical and corrosion properties of commercial WE43 alloy prepared by various processing techniques including conventional casting, extrusion, and powder metallurgy methods such as spark plasma sintering. For different processing technique, differences in microstructures were observed, including different grain sizes, intermetallic phases, amount of alloying elements in the solid solutions, or specific structural elements. Mechanical and corrosion properties were improved especially by grain refinement. Precipitation from oversaturated solid solutions led to further improvement of mechanical properties, while corrosion resistance was just slightly decreased due to the fine and homogeneously distributed precipitates of $Mg_{41}Nd_5$. The obtained results indicate huge differences in ignition resistance based on the metallurgical state of the microstructure. An improved ignition resistance was obtained at the condition with a higher concentration of proper alloying elements (Y, Nd, Gd, Dy) in the solid solution and absence of eutectic phases in the microstructure. Thermally stable intermetallic phases had a minor effect on resulting ignition temperature.

Keywords: WE43 alloy; gravity casting c; extrusion; SPS; microstructure; mechanical properties; ignition temperature

1. Introduction

Magnesium alloys are interesting in two different fields—biomaterials and industry. The possibility of reduction of transportation costs led to the increased interest in lightweight materials. Magnesium alloys as light materials with good mechanical properties are highly demanded in the automotive, railway, and aerospace industries [1]. The density of magnesium is 1.74 g/cm^3 which is 35% and 75% lower than aluminum and iron, respectively, which are the metals used for construction [2,3]. The replacement of aluminum parts with magnesium would cause a reduction of the weight of an airplane by up to 30% [4]. Such a reduction of weight would, therefore, result in the reduction of the burnt fuel and subsequently reduced CO_2 emissions [5].

The great danger of processing the magnesium alloy lies in the possibility of combustion during the melting and casting [6,7]. Magnesium has a high affinity to oxygen and is characterized by high vapor pressure [8]. The magnesium oxide which is created on the surface of the molten material has no protective ability [9]. Therefore, protective gases such as SF_6 have to be used for melt protection [10,11].

Researchers tried to identify ignition retarding alloying elements which would protect the melt without the necessity of cover gas or flux. It was investigated that some elements significantly improve resistance to oxidation. Ca, Be, Gd, Y, and Nd are among these elements [9,10,12]. These elements are more reactive with oxide than magnesium. Thus, a

dense protective layer of such oxides can be formed on the surface. The properties of the layer depend on the amount of dissolved elements in the magnesium matrix as well as on the Pilling–Bedworth ratio (PBR) and the Gibbs free energy change for oxidation [10,13]. The PBR is a ratio of the volume of newly created oxide to the volume of original metal material from which the oxide was created. Generally, it represents the volume change during oxidation. If the PBR is between 1 and 2 then the oxide layer sufficiently prevents the surface from further oxidation of the bulk. A higher value leads to the creation of cracks, while a lower value results in a porous oxide layer [13]. The impact of alloying elements on the oxidation and ignition temperature is summarized in Table 1 by Kim et al. [13] who compared the influence of PBR, solubility limit, and Gibbs free energy change for oxidation on the ignition temperature for different alloying elements. One can see that ignition temperature could not be easily estimated just from PBR or Gibbs free energy alone. Generally, high Gibbs energy together with low solubility decrease ignition temperature, contrary, low Gibbs energy with high solubility greatly increases the ignition temperature. Chen et al. [14] investigated the positive effect of rare earth elements (REEs) in AZ91D magnesium alloy. Even a small amount (0.1 wt % of REEs) was enough to increase the ignition temperature by up to 250 °C [15]. Neodymium should form a protective layer of Nd_2O_3 which also improves ignition temperature by up to 140 °C for the binary alloy with 2 wt % of Nd [8]. Nevertheless, researchers agree that the ignition temperature is reduced only if the amount of alloying elements is above a certain limit. The limit is usually associated with the solubility of the element in the magnesium matrix as intermetallic phases have a lesser influence on the ignition properties.

Table 1. Effect of individual properties of alloying elements on the ignition temperature [13].

Alloy	T_{ig} (°C)	Oxide	PBR	The Solubility Limit of the Element (wt %)	ΔG (J, at 700°C) *
Mg-0.55Y	721	Y_2O_3	1.13	3.4	−133
Mg-0.48Gd	707	Gd_2O_3	1.29	4.53	−56
Mg-1.46Dy	726	Dy_2O_3	1.26	4.83	−87
Mg-1.42Er	762	Er_2O_3	1.20	6.91	−125
Mg	504	MgO	0.81		

* Gibbs free energy change in the reaction of $aMgO + bX \rightarrow XbOa + aMg$.

Magnesium alloys are generally characterized by three major disadvantages which limit their application. One of them is a high corrosion rate, the second one is low creep resistance and quick loss of mechanical properties at higher temperatures and the third one is a low temperature of ignition, high burning temperature, and therefore problematic extinguishing, which was the main reason behind the recently canceled ban of magnesium alloys in the interiors of the planes [1,2]. However, the proposed materials have to pass the ignition tests. Therefore, there was an effort of many scientists to measure ignition temperatures of the most widely used magnesium alloys [11]. Researchers varied in the methods used for the determination of the ignition temperature. The ignition temperature was identified by the sudden increase of temperature due to the burning of the sample [16]. Ming Liu et al. [17] measured ignition temperature by the simple furnace test and measured a relatively low ignition temperature of 644 °C for WE43 alloy. This value was lower by almost a hundred degrees compared to the value obtained by Kumar et al. [18] (730 °C) who measured the ignition temperature of the same alloy in an induction furnace on air. This difference confirms that the presence of oxygen is an important factor for the creation of protective films. Results of the test from the Federal Aviation Administration (FAA) indicate that the WE43 and ZE10 alloys have similar ignition properties to aluminum alloys [1]. Both alloys have the ability of self-extinguishing when removed from the source of the fire. Eyring and Zwolinski [19] found out that the heat conduction from the oxide

surface has also a positive influence on the ignition temperature. A significant amount of magnesium vapor during melting allows it to burn easily [8]. On the other hand, the ignition can be stopped by sufficient heat extraction [19]. Bungaro et al. [20] investigated the incorporation of oxygen beneath the surface of the magnesium matrix. According to the calculations of Shröder et al. [21], the isolated oxygen atoms tend to be absorbed on the surface, while large clusters of oxygen atoms are driven below the magnesium surface into the bulk. Another method for the determination of ignition temperature is a flame test, where the specimen is subjected to the direct flame. This approach is suitable to simulate the real scenario of fire in the aircraft [16].

WE43 alloy contains approximately 4 wt % of Y and 3 wt % of REEs which include Nd, Gd, Dy, and Zr. This material is usually prepared by casting and subsequent thermo-mechanical processing. The heat treatment T4 is performed at 525 °C for 8 h followed by quenching in water in order to dissolve eutectic β phase $Mg_{14}Nd_2Y$. This material can be subsequently aged at 250 °C for 16 h. During this period new phases precipitate, such as β″ (orthorhombic, metastable phase), β′ (D019, metastable phase), β ($Mg_{14}Nd_2Y$) [22,23], $Mg_{24}Y_5$, Mg_3Nd, $Mg_{12}Nd$, and $Mg_{41}Nd_5$ [24–27]. The precipitation leads to the improvement of mechanical properties with values of 140–170 MPa for tensile yield strength and 4–7% for elongation in the T6 state [22]. Corrosion properties strongly depend on the morphology, distribution and shape of the phases. Most intermetallic phases in the WE43 alloy have a corrosion potential close to the Mg matrix, which reduces the effect of galvanic corrosion [27]. Microgalvanic corrosion is a problem of magnesium alloys containing other elements than REEs [28,29]. Moreover, it was found that the $Mg_{41}Nd_5$ phase has even more negative potential than the surrounding matrix or phases, which improves the overall corrosion resistance [30,31]. The highest difference in potential is between Mg matrix and Zr-rich phases, thus these phases are the most problematic in WE43 alloy from the corrosion point of view [27].

This work focuses on the WE43 alloy with acceptable ignition-proof properties according to the FAA. Recent publications deal with many novel alloys with improved ignition properties. They focus on the alloying elements while the effect of processing is omitted. Therefore, in this paper, the well-known advanced WE43 alloy was prepared by different methods in order to investigate the possible effect of the preparation method on microstructure, mechanical, corrosion, and especially ignition properties. The results may serve as a tool for choosing the right preparation method of novel alloys with improved ignition properties. This paper showed a possible improvement of ignition temperature by up to 230 °C caused by processing.

2. Materials and Methods

2.1. Sample Preparation

Samples were prepared by several different methods. Commercial WE43 bulk alloy was re-melted in the induction furnace at 750 °C for 0.5 h under a protective argon atmosphere (99.96%). The melt was cast into the cold brass mold with 50 mm in diameter (As-cast state, AC). As-cast ingot was solution treated at 525 °C for 8 h with subsequent quenching in the water (T4 state). Both as-cast and heat-treated ingots were extruded at 400 °C with an extrusion ratio of 10 and an extrusion rate of 5 mm·min^{-1}. Commercial atomized powder of WE43 alloy with arithmetic mean diameter of 80 µm and the size distribution shown in Figure 1 was cold pressed at 80 kN into cylinders with 20 mm in diameter. Such a green compact was extruded at the same conditions as ingots (P + Ex). As an alternative way of preparation, the powder was also compacted by the spark plasma sintering (SPS) method. The powder was pressed at 32 MPa at the temperature of 500 °C for 10 min with a heating rate of 100 °C min^{-1}. The final material was a cylinder with 20 mm in diameter and a height of 15 mm. The composition of ingot and powder according to inductively coupled plasma mass spectrometry ICP-MS (Elan DRC-e, PerkinElmer, Waltham, MA, USA) is given in Table 2.
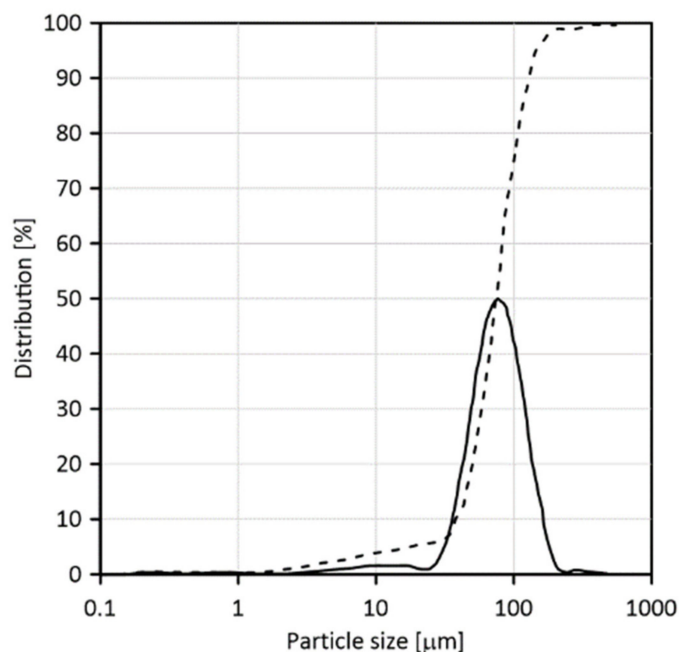
Figure 1. Powder size distribution. [32]. Reprinted with permission from ref. [32]. Copyright 2020 Elsevier.

**Table 2.** The composition of ingot and atomized powder with dangerous trace elements.

Sample	Composition (wt %)						Impurities (ppm)		
	Mg	Y	Nd	Dy	Gd	Zr	Fe	Ni	Cu
WE43 Ingot	Bal.	3.6	2.2	0.3	0.3	0.4	16	5	23
WE43 Powder	Bal.	4.0	2.2	0.4	0.4	0.5	32	13	29

2.2. Microstructure Characterization

The compacted products were ground on SiC papers P80-P2500 and polished on a diamond paste D3. The final polishing was performed on an Eposil F suspension. The microstructure was characterized by scanning electron microscope SEM TescanVEGA3 with energy dispersion spectrometry (EDS, AZtec Tescan, Brno, Czech Republic). EDS point or area analyses were used for the estimation of composition of solid solution or intermetallic phases. Phase analyses were performed using X-ray diffraction (XRD, X'Pert Philips, 30 mA, 40 kV, CuKα X-ray radiation, PANanalytical, Almelo, Netherland). The grain size was determined by image analysis (diameter) after etching of the samples in the solution containing 10 mL of acetic acid, 4.2 g of picric acid, 10 mL of distilled water, and 70 mL of ethanol.

2.3. Mechanical Properties

The compressive and tensile mechanical properties were measured. For both tests, the constant strain rate of 0.001 s^{-1} was selected. The samples for the compressive properties were cylinders with a diameter of 5 mm and a height of 8 mm (Figure 2B). Compressive yield strength (CYS), ultimate compressive strength (UCS), and relative deformation (D) were evaluated. Samples for the tensile tests were 25 mm long and had 3.5 mm in diameter in the narrowed area (Figure 2A). Tensile yield strength (TYS), ultimate tensile strength (UTS), and elongation (A) were evaluated. The samples for the compressive tests prepared by casting and SPS process were rectangular with dimensions of 8 mm × 5 mm × 5 mm (Figure 2C). For tensile tests of SPS products, bone-shaped samples that were 2 mm × 4 mm thick and 10 mm long in the gauge area were used due to the small size of the compacted sample (Figure 2D).
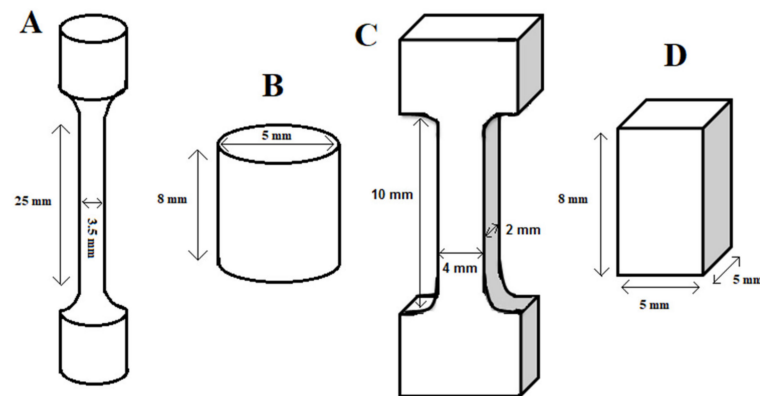
Figure 2. Dimensions of samples for testing: (**A**) Ingot and extruded specimens for tensile tests, (**B**) Ingot and extruded specimens for compressive and corrosion tests, (**C**) SPS specimen for tensile test, (**D**) SPS specimen for compressive and corrosion tests.

2.4. Corrosion Properties

WE43 alloy is also considered a suitable biomaterial, therefore, must show a reasonable corrosion rate to serve as a biomaterial. The human environment is more aggressive than atmospheric conditions, therefore, corrosion tests were performed in simulated body fluid at 37 °C for 14 days. In the case of extruded samples, cylindrical samples with a diameter of 5 mm and height of 8 mm (Figure 2B) were used, while rectangular samples with dimensions of 8 mm × 5 mm × 5 mm (Figure 2D) were prepared in the case of casted ingots and SPS products. The samples were ground on P2500 papers and rinsed in ethanol and acetone. Samples were mounted into plastic holders and exposed for 14 days. Afterwards, samples were rinsed with distilled water, and the corrosion products were removed in the solution of 200 g/L CrO_3, 10 g/L $AgNO_3$, 20 g/L $Ba(NO_3)_2$. The corrosion rate was calculated in $mm \cdot a^{-1}$ from the weight changes between original conditions and after the removal of the corrosion products. The corrosion rate was calculated according to Equation (1):

$$v_{cor}\left[\text{mm·a}^{-1}\right] = \frac{\Delta m \text{ [g]} \cdot 10 \cdot 365 \text{ [days]}}{d \text{ [days]} \cdot S \text{ [cm}^2] \cdot \rho_{Mg} \text{[g·cm}^{-3}]} \tag{1}$$

where Δm is a weight change after removal of corrosion products, d is the number of days of exposition, S is the surface area of the sample and ρ_{Mg} is the density of magnesium.

2.5. Ignition Temperature Measurement

For the evaluation of ignition temperature samples with dimensions of 15 mm × 15 mm × 5 mm were ground on P1200 SiC papers and put into an Al_2O_3 crucible. The crucible was inserted into the resistance furnace. The thermocouple was in direct contact with the sample. Technical air with airflow of 100 $L \cdot h^{-1}$ was blowing into the crucible. The heat rate of the furnace was set to 30 $°C \cdot min^{-1}$. The ignition temperature was evaluated from the temperature vs time diagrams. The sudden increase of the temperature due to the ignition of the sample was proclaimed as ignition temperature. Each sample was measured three times.

2.6. Analysis of Oxide Mechanism

For the analysis of oxide layers, the crucible with the sample was removed from the resistance furnace at 650 and 800 °C and cooled on air. The oxide layer which was formed on the surface was studied by SEM with EDS and by X-ray diffraction.

3. Results and Discussion

3.1. Microstructure Characterization

WE43 alloy was successfully prepared by several different processes. Four materials were prepared from the commercially available cast ingot and the remaining two from the commercially available atomized powder. The microstructure of the cast ingot has a typical dendritic microstructure with visible segregation at grain boundaries (Figure 3A,D).
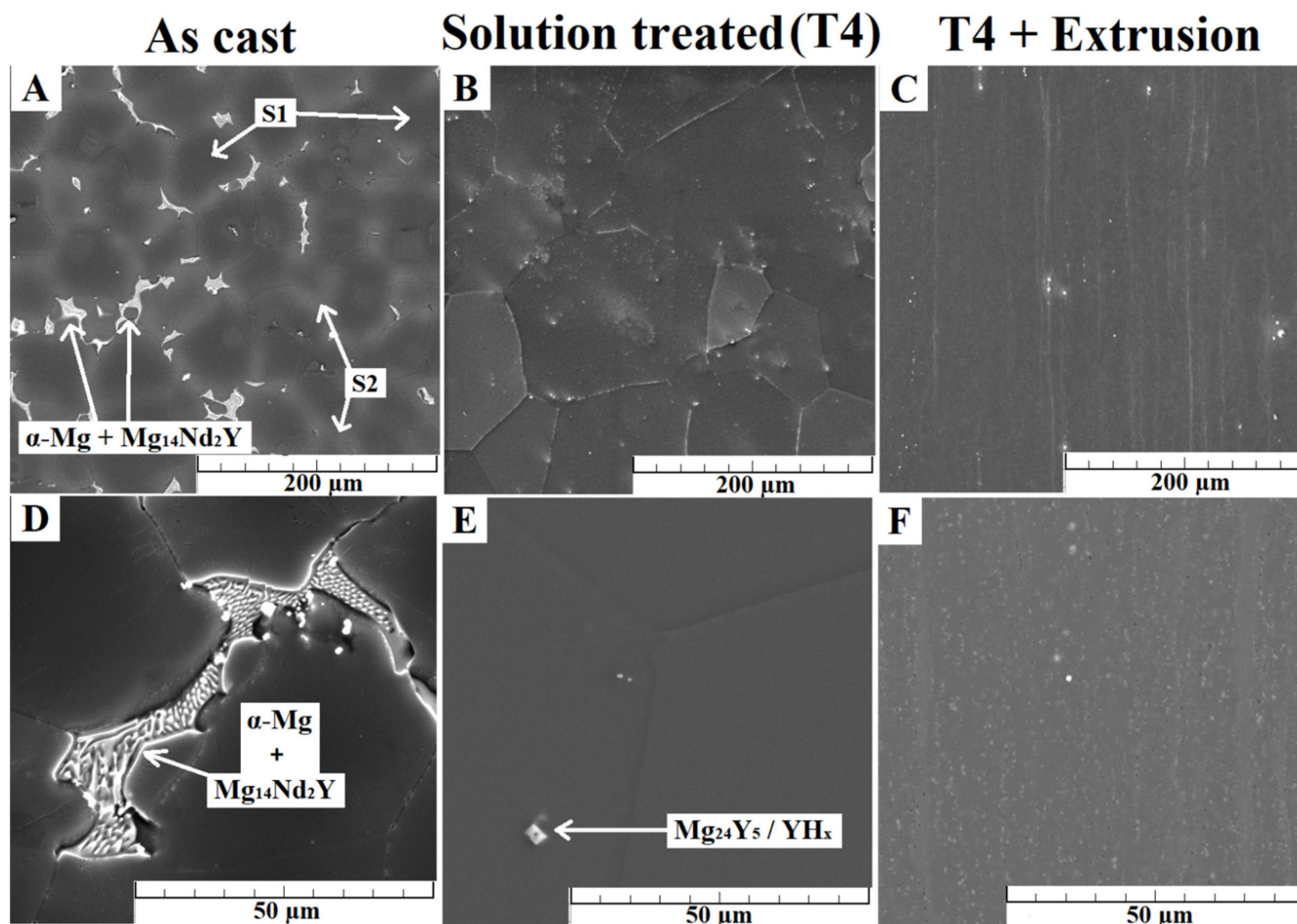
Figure 3. Microstructures of the WE43 alloy prepared by different processes: As-cast (**A,D**); Solution treated—T4 (**B,E**); Solution treated—T4 + extrusion (**C,F**).

The microstructure consists of α-Mg solid solution and eutectic β phase $Mg_{14}Nd_2Y$ (12 ± 1 wt % of Y, 28 ± 1 wt % of Nd, and 1–2 wt % of Gd and Dy). Additionally, other binary phases such as $Mg_{24}Y_5$, Mg_3Nd, and $Mg_{12}Nd$ were observed by XRD (Figure 4) which is in accordance with findings in the literature [24–27]. Although not evident in the XRD spectrum, small cubic-shaped particles in microstructure were analyzed as YH_x hydrides according to EDS results. A similar observation was confirmed in various publications [25,33,34]. The solid solution (S1) contained 2.1 ± 0.3 wt % Y, 1.0 ± 0.1 wt % Nd, 0.6 ± 0.2 wt % Zr, 0.2 ± 0.1 wt % Dy, 0.2 ± 0.1 wt % Gd. The segregation areas (S2) contained 5.5 ± 0.4 wt % Y, 2.5 ± 0.3 wt % Nd, 0.3 ± 0.1 wt % Zr, 0.5 ± 0.1 wt % Dy, 0.5 ± 0.1 wt % Gd. The grain size of this material was between 20 and 100 μm, which is slightly higher compared to the observation of Jiang et al. [24] due to the lower cooling rate of as-cast alloy in the presented state.
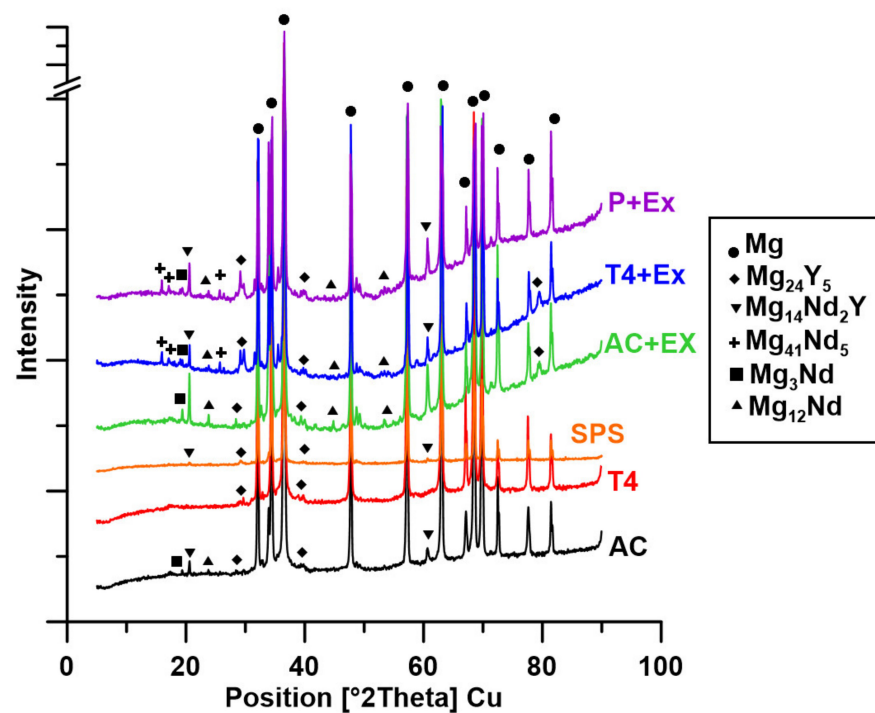
Figure 4. XRD of the prepared materials.

The eutectic phase completely dissolved after solution treatment (T4). Only thermally stable phases remained in the microstructure (Figure 3B,E). Those phases were $Mg_{24}Y_5$ and probably $Mg_{12}Nd$, and YH_x hydrides which were not detected by XRD due to their low content and isomorphic behavior (Figure 4) but assigned to according to the EDS analysis [34]. The solid solution was therefore rich in alloying elements (Table 3). Elevated temperature caused the grain growth which was to some extent retarded by the present phases. The final grain size was between 50 and 200 μm.

**Table 3.** The grain size and amount of alloying elements in the solid solution measured by EDS analysis (wt %).

Material	Y	Nd	Gd	Dy	Zr	Sum	Grain Size [μm]
As-cast (dark)	2.1 ± 0.3	1.0 ± 0.1	0.2 ± 0.1	0.2 ± 0.1	0.5 ± 0.1	4.0	78
As-cast (bright)	5.5 ± 0.4	2.5 ± 0.3	0.5 ± 0.1	0.5 ± 0.1	0.3 ± 0.1	9.3	78
T4	3.8 ± 0.2	2.2 ± 0.2	0.3 ± 0.1	0.3 ± 0.1	0.4 ± 0.1	7.1	138
Ex	2.8 ± 0.3	1.2 ± 0.1	0.2 ± 0.1	0.3 ± 0.1	0.5 ± 0.1	5.1	3.3
T4Ex *	4.3 ± 0.2	2.2 ± 0.2	0.4 ± 0.1	0.4 ± 0.1	0.4 ± 0.1	7.8	2.6
PEx *	4.2 ± 0.2	2.2 ± 0.3	0.4 ± 0.1	0.4 ± 0.1	0.9 ± 0.1	8.1	1.8
SPS *	4.0 ± 0.1	2.4 ± 0.1	0.4 ± 0.1	0.5 ± 0.1	0.8 ± 0.1	8.2	5.9

* Measured values affected by precipitation

The extrusion of the heat-treated sample resulted in quite a homogeneous microstructure containing fine intermediate phases, which remained in the microstructure after T4 or precipitated from the solid solution during extrusion (Figure 3C,F). Intermetallic phases were ordered in rows parallel to the extrusion direction. Detected phases were $Mg_{24}Y_5$, $Mg_{12}Nd$, $Mg_{41}Nd_5$, Mg_3Nd, and $Mg_{14}Nd_2Y$ (Figure 4). Interestingly, the $Mg_{41}Nd_5$ phase was observed only in heat-treated ingot processed by extrusion and atomized powder processed into a compact by extrusion. Thus, this phase is probably associated with the precipitation process as both materials have initially supersaturated solid solutions [35]. The composition of the solid solution is given in Table 1 but due to the distinctiveness of

EDS and dense distribution of precipitates, this has to be taken with caution. Dynamic recrystallization occurred during the extrusion and the final grain size was between 0.5 and 8 μm.

The forward extrusion of the as-cast ingot resulted in the microstructure presented in Figure 5A,D. The eutectic phase was partially dissolved in the solid solution and the rest was ordered in rows parallel to the extrusion direction. There were $Mg_{14}Nd_2Y$, Mg_3Nd, $Mg_{12}Nd$, and $Mg_{24}Y_5$ among observed phases (Figure 4). All of those phases were observed in the as-cast state. Presented phases were much larger compared to the phases in the rod prepared by extrusion from the solution-treated ingot. The composition of the solid solution was slightly different due to the presence of a higher amount of alloying elements in intermetallic phases (Table 3). The grain size was reduced due to recrystallization and was in the range of 0.5–10 μm.
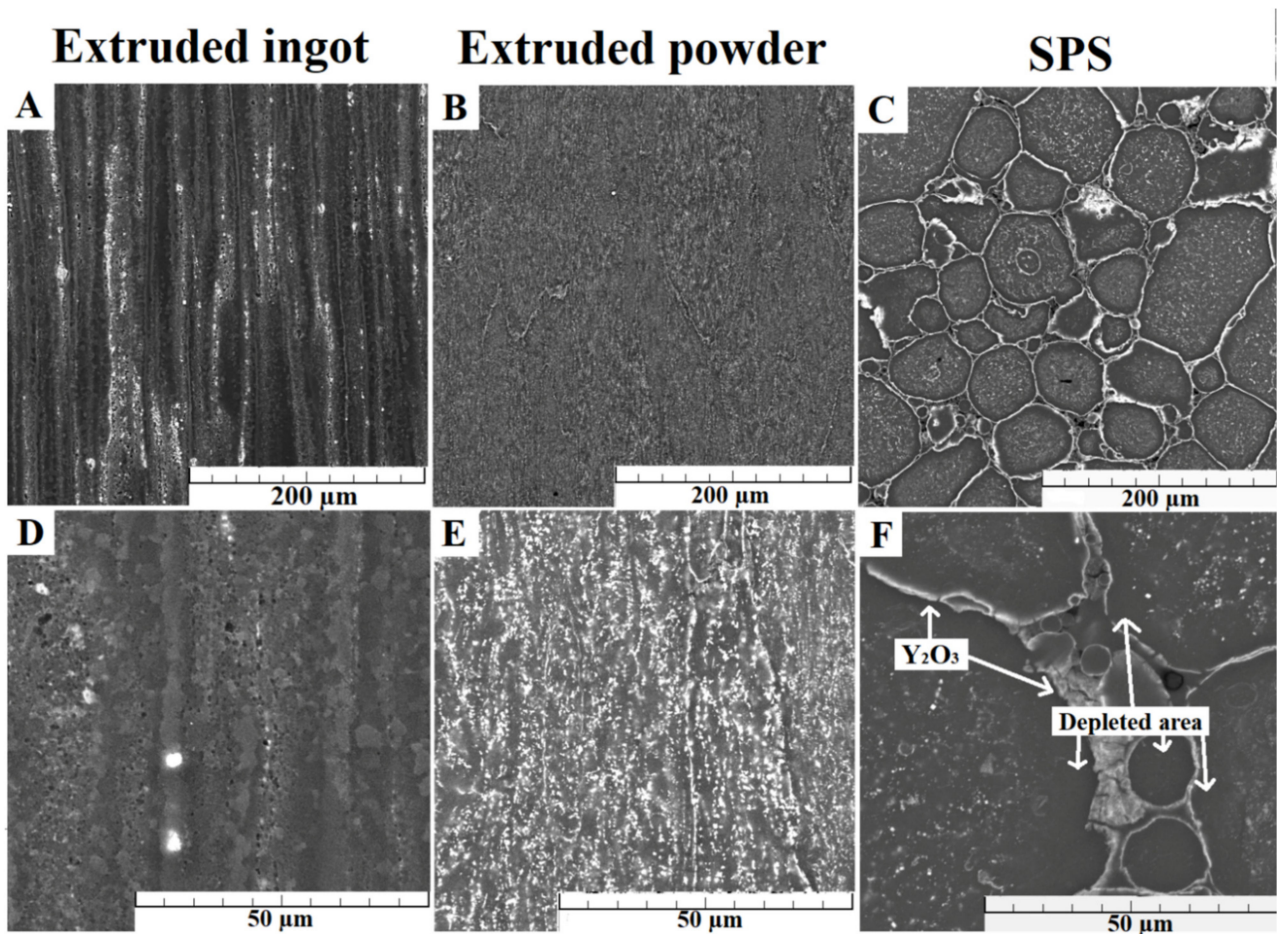
Figure 5. Microstructures of samples prepared by extrusion of ingot (**A,D**); extrusion of powder (**B,E**); SPS (**C,F**).

The microstructure of the material prepared by the extrusion of green compact from WE43 powder is displayed in Figure 5B,E. There are still partially visible borders between original particles of atomized powder. Otherwise, the microstructure contains a high amount of fine intermetallic phases which precipitated from the supersaturated solid solution of atomized powder. These phases were identified as $Mg_{14}Nd_2Y$, $Mg_{41}Nd_5$, Mg_3Nd, and $Mg_{24}Y_5$ (Figure 4) where the newly observed $Mg_{41}Nd_5$ phase suggests a precipitation process as an atomized powder contained supersaturated solid solution before extrusion. The composition of the solid solution is given in Table 3 but due to the distinctiveness of EDS and dense distribution of precipitates, this has to be taken with caution. The grain size was slightly lower than for other materials between 0.5 and 5 μm probably due to the pinning effect of presented phases in powder during extrusion and therefore grain growth suppression.

The last sample was prepared by SPS which allows very fast compaction of the powder. The sample was exposed to higher temperature only for several minutes. One can see those individual powder particles are surrounded by a thick oxide shell that was created during sintering (Figure 5C,F). There was residual trapped air between powder particles which allowed the surface oxidation of individual particles. The formation of oxide shell consumed Y in the near surroundings of the surface as has been already suggested in the literature [32,33,36–39]. The original dendritic microstructure in atomized powder turned into a homogenous microstructure with fine precipitates similar to the T4Ex state. The intermetallic phases were identified as $Mg_{14}Nd_2Y$ and $Mg_{24}Y_5$ (Figure 4), which suggests only limited precipitation of the $Mg_{14}Nd_2Y$ phase, which was probably created from the metastable β^1 phase which was in the atomized powder [23]. The solid solution contained 4.0 ± 0.1 wt % Y, 2.4 ± 0.1 wt % Nd, 0.8 ± 0.1 wt % Zr, 0.5 ± 0.1 wt % Dy, 0.4 ± 0.1 wt % Gd except for the area near the borders of original powder particles, which was depleted by Y. The grain size ranged between 1 and 10 μm.

3.2. Mechanical Properties

The compressive (A) and tensile (B) properties of all prepared materials are summarized in Figure 6. There are relatively small differences between compressive properties and tensile properties related to the same kind of material. The materials prepared from cast and heat-treated ingot were characterized with the lowest tensile strengths due to the large grain size. After heat treatment, the intermetallic phases dissolved into the solid solution, however, the expected decrease of mechanical properties due to the reduced particle strengthening effect was compensated by solid solution strengthening.
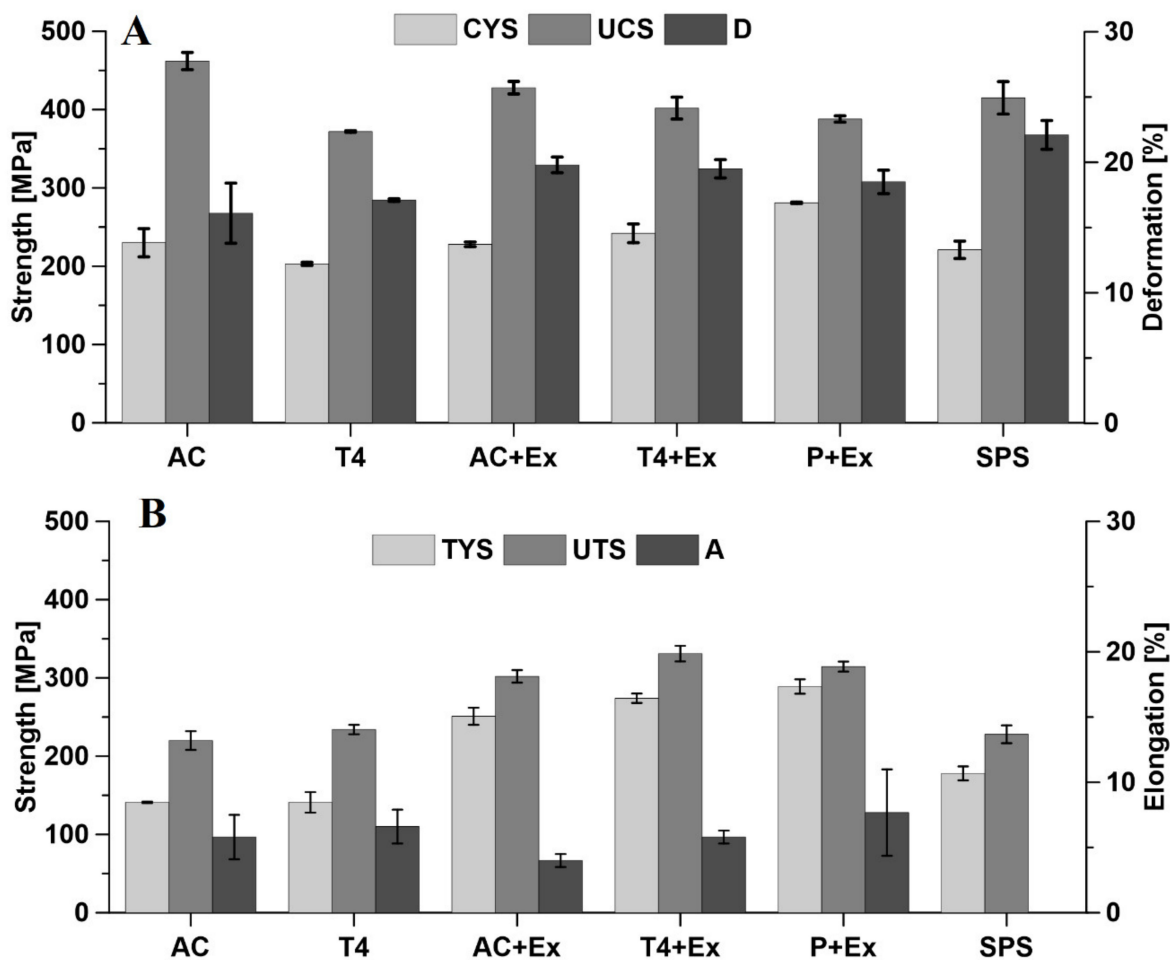

Figure 6. Compressive (**A**) and tensile (**B**) properties of prepared materials.

Although the SPS products were characterized by relatively small grain size, the mechanical properties were lower compared to the extruded samples. Such difference is associated with interfaces between powder particles. These interfaces containing predominantly Y_2O_3 were fragile and led to a decrease in mechanical properties. Unfortunately, due to the small sample size, it was not possible to measure the elongation to fracture with an extensometer.

The extruded materials exerted superior mechanical properties, especially due to the small grain size in accordance with the Hall–Petch behavior. The improved properties of the material prepared from the heat-treated ingot are associated with better homogeneity, increased amount of alloying elements in the solid solution, and occurrence of fine precipitates in the microstructure of extruded sample [40].

Generally, compressive strength is usually higher compared to tensile strength, as possible defects have a greater effect in tension [41–43]. However, both extruded ingots reached the opposite results. Interestingly, the extruded green compact from the powder exerted almost the same compressive and tensile strength. This might be associated with the occurrence of texture in the material. Magnesium is known to form a texture after deformation when newly recrystallized grains usually tend to orient themselves with basal planes parallel to the extrusion direction. This orientation favors the compression twining under compression along the extrusion axis, which requires less energy than the slip mechanism, and therefore, the measured compressive yield strength is lower than tensile yield strength [41–44]. It has been shown that the powder metallurgy products are characterized by weaker texture, and therefore, they exert lower anisotropy of mechanical properties [22].

The measured values of the tensile yield strengths are dependent on the grain size according to the Hall–Petch relation which is enumerated in Equation (2) and displayed in Figure 7.

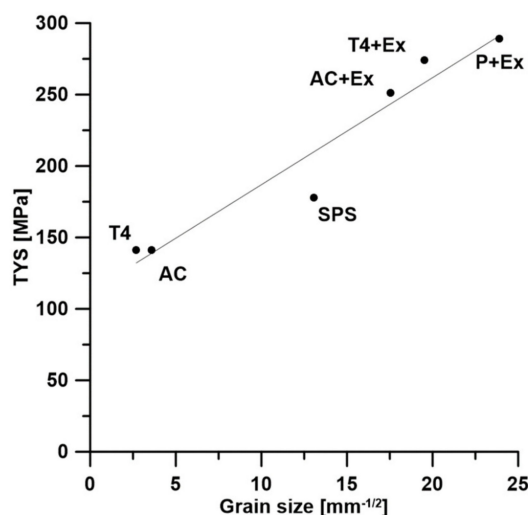$$TYS = 112 + 7.5 \cdot d^{-\frac{1}{2}} \tag{2}$$

Figure 7. Hall–Petch relation.

Although, there are deviations from this relation related to other causes such as solid solution strengthening, strengthening by precipitates, texture, and inhomogeneities. The effect of solid solution strengthening is visible in the case of heat-treated ingot (T4) as it reached the same value of TYS as cast ingot (AC) even though the grain size was larger and also there was no strengthening by intermetallic phases. A great negative deviation was detected for the SPS product. This is associated with inhomogeneous microstructure with brittle oxide interfaces between original powder particles. Both extruded ingots were characterized with anisotropy of mechanical properties associated with texture, therefore,

the positive deviation is caused by texture strengthening. This was not observed for powder metallurgy product with the lowest anisotropy of TYS/CYS, and therefore the lowest expected texture strength. Jiang et al. [24] calculated the Hall–Petch relation for WE43 alloy and they measured a lower value of the constant which was equal to 95 MPa, on the other hand, the coefficient was higher and equal to 350 MPa·μm$^{1/2}$. Different values might be associated with the different preparation process consisting of casting and heat treatment. The constant equal to 112 MPa in the Hall–Petch relation (2) is higher than in the case of Mg-3Nd-0.5Zn alloy [45], which represents higher initial strength due to the higher amount of alloying elements in material and stronger strengthening by solid solution and/or intermetallic phases. Moreover, a lower coefficient (7.5 MPa·mm$^{1/2}$ or 237·μm$^{1/2}$ MPa) suggests minor dependency on the grain size [46].

The measured mechanical properties of cast and heat-treated ingots were comparable with the observations in the literature [24,25,47,48]. The extruded samples exerted slightly better tensile properties compared to the literature [49–52] which is associated especially with finer grain size.

3.3. Corrosion Properties

The values of corrosion rate calculated out of the weight changes after exposition in SBF solution are listed in Table 4. Generally, improved corrosion resistance of WE43 alloy is associated with the formation of more stable corrosion products based on Y such as Y_2O_3 or $Y(OH)_3$ [53]. Those products can be more easily formed from the solid solution rich in Y.

Table 4. The corrosion rate in SBF [mm·a^{-1}].

As-cast	T4	Ex	T4+Ex	P+Ex	SPS
1.78 ± 0.07	0.82 ± 0.24	0.63 ± 0.05	0.53 ± 0.32	0.58 ± 0.11	3.15 ± 0.27

The highest corrosion rate was measured for the SPS product. This behavior is related to the specific interface between original powder particles where the Y_2O_3 shell is present but its surroundings are depleted by Y. The inhomogeneity inside powder particles caused rapid corrosion [32,36,37].

The inhomogeneity of chemical composition due to the segregation in the as-cast ingot and the presence of large intermetallic phases which together with Mg matrix formed microgalvanic cells also led to the fast degradation. After heat treatment, the intermetallic phases dissolved into the solid solution. The near absence of intermetallic phases together with a high amount of alloying elements in the solid solution noticeably improved corrosion resistance.

Nevertheless, extruded samples exerted superior corrosion resistance especially due to the grain refinement [54]. The grain boundary is considered as a defect and therefore, it is prone to corrosion. Smaller grain size increases the amount and density of these defects which work as anodic sites. This leads to faster passivation of grain interior and, due to the concomitant increase of pH at grain boundary, to general lowering of the overall corrosion rate. Additionally, due to small grain size, the mismatch between crystal structures of Mg matrix and protective oxide film is reduced, which results in lower tension in the layer of corrosion products [30]. The T4 heat treatment before extrusion led to the homogenization of microstructure and therefore the corrosion rate of subsequently extruded material was slightly lower compared to the material prepared by the extrusion of the as-cast ingot. Atomization of WE43 caused the formation of supersaturated solid solutions in powder. After extrusion, a high concentration of REEs in solid solution was slightly depleted, and new small particles were precipitated homogeneously in material and close to each other, suppressing the effect of microgalvanic cell. In both cases, $Mg_{41}Nd_5$ phase was observed. It was shown that this phase can be dissolved preferentially due to the more negative potential compared to the Mg matrix. Moreover, homogeneous distribution of fine $Mg_{41}Nd_5$ phases leads to the overall improved corrosion resistance [30,31]. Finally,

almost similar corrosion resistance of extruded powder compared to the T4-Ex sample was observed.

In comparison to the literature sources, measured values of corrosion rates in this work are in the range of measured corrosion rates of WE43 alloy in various environments and states. Zhang et al. [49] reached a lower value of corrosion rate (0.26 mm·a^{-1}) which might be associated with the lower ratio of corrosive medium to the surface area which allows faster rise of pH and easier passivation. Contrary, Li et al. [55] measured a high corrosion rate of 2 mm·a^{-1} for extruded WE43 alloy with a ratio of 5 dm^3 of Hank's solution per 1 cm^2 of surface area. For industrial application, the corrosion rate of 0.24 mm·a^{-1} in a 3.5 wt % solution of NaCl was measured by Argade et al. [56]. In this case, measured lower corrosion rate is associated with a longer time of exposition as the material degrades fast initially, and then it is retarded by the formation of stable corrosion products. Yang et al. [27] measured a similar corrosion rate of approximately 1.8 mm·a^{-1} and 0.5 mm·a^{-1} in 3.5 wt % solution of NaCl for as-cast WE43 alloy, and aged hot rolled WE43 alloy respectively. Corrosion rates of extruded products in this work are therefore acceptable for bioapplication.

3.4. Ignition Temperature Characterization

Ignition temperatures were measured in the furnace with the inflow of technical air. The curves of temperature versus time were evaluated and at the point of a sudden increase of temperature, the ignition temperature was determined. The average values calculated from the six measurements are summarized in Table 5. Alloying elements in the WE43 alloy greatly improve ignition temperature by 200 °C compared to pure Mg. This is the main reason why WE43 is approved by FAA to be used in the aviation industry. An increase of ignition temperature is associated with the formation of a stable oxide layer on the surface of the material during heating. The stability and probability of the formation of such a layer depend on several parameters. Alloying elements with at least limited solubility in Mg react with oxygen preferably compared to magnesium matrix and thus have usually a protective effect. Except Ca, the greatest improvement is known for Y, Nd, and Gd. A formed thin layer of Y_2O_3, Nd_2O_3, and Gd_2O_3 on the surface protects even the molten alloy at temperatures above the melting point of magnesium. The amount and type of alloying elements have a great effect on the ignition temperature.

Table 5. Ignition temperatures of WE43 alloy prepared by different processes [°C].

As-cast	T4	Ex	T4+Ex	P+Ex	SPS
855 ± 36	1082 ± 11	1000 ± 17	1024 ± 6	936 ± 6	994 ± 28

Nevertheless, according to Table 5, a great dependency of ignition temperature on the processing method is evident. Solution treatment (T4) of the WE43 alloy can further increase the ignition temperature by 200 °C compared to the as-cast state. This effect is associated with the amount of alloying elements in the solid solution. The initial protective layer is formed from the elements in the solid solution while stable intermetallic phases usually stay unchanged at the beginning of heating. The main issue of as-cast material is the existence of a eutectic mixture. This mixture melts easily at a temperature of about 570 °C leading to the disruption of oxide films on the surface of the material due to the volume changes connected to the solid–liquid state. Other materials contained intermetallic phases stable to higher temperatures which transformed into the liquid state only after melting of the matrix. These stable phases support the formation of the protective oxide layer (Y, Nd, Gd, Dy) by release of alloying elements during dissolution and diffusion. It is clearly visible that all states except as-cast condition are characterized by closer values of ignition temperature, which is related to the closer conditions of the initial microstructure. Only the P+Ex state is characterized by an ignition temperature somewhere between as-cast and other states, however, this could be connected to the lower concentration of alloying elements in solid solution due to the existence of a high amount of intermetallic phases in the microstructure. The solution treatment dissolved secondary phases and significantly

increased the amount of Y in the solid solution from 2.1 to 3.8 wt %. This allowed an easier formation of homogeneous Y_2O_3 on the surface from the beginning of the exposition even in the solid state of the material.

Subsequent extrusion of the T4 heat-treated ingot resulted in a small decrease of ignition temperature. We believe that it is connected to the precipitation during extrusion and therefore depletion of solid solution. This will affect the formation of surface oxide up to the melting of alloys. It is likely that also the interface of oxide and alloys is affected by the presence of precipitates which may increase the stresses in the oxide layer and therefore decrease its strength [57]. On the contrary, the ignition temperature increased by 150 °C for material extruded from the as-cast ingot due to the homogenization of microstructure during extrusion (removing of dendritic microsegregation). The materials homogeneity of the microstructure was also the reason behind the lower deviation of measured values compared to as-cast ingot.

The selection of the powder metallurgy method led to the lower ignition temperature compared to the extruded materials. Such behavior is attributed to the huge amount of intermetallic phases which willingly precipitated out of the supersaturated solid solution during extrusion. These phases disrupt the interface between magnesium matrix and oxide and therefore may increase the stresses in the oxide layer, and therefore, decrease its strength. Nevertheless, the value of ignition temperature was still higher by 80 °C compared to the as-cast ingot, which is related to the more homogenous microstructure conditions.

The material prepared by the SPS method exerted ignition temperature 994 °C. This material contained a lower density of intermediate particles in the microstructure which had a positive effect on ignition resistance compared to the PEx material. On the contrary, the inhomogeneity due to the depletion of Y at the particle borders led to the lower observed ignition resistance compared to the T4 and extruded materials.

It is interesting that an almost 230 °C difference in ignition temperature may be observed based on the processing methods and related microstructure conditions in the solid state. Although the burning of Mg-based alloys takes place generally in the liquid state, it seems that the effect of microstructure conditions is underestimated. The effect of microstructure on ignition temperatures may vary for other materials due to the different solubility of elements in solid solution or the occurrence of various intermetallic phases. The ignition temperature may also decrease after thermomechanical processing as was measured for Mg-0.5Y-0.5Gd-0.5Ca alloy in the as-cast and extruded conditions. This decrease was, however, negligible at ~20 °C [58,59].

Nevertheless, WE43 alloy proved to be an advanced commercial alloy for various applications as the measured ignition temperature in selected conditions was comparable or superior to other magnesium alloys designed such as highly ignition resistant materials [6,8,11–13,16,17,60].

3.5. Oxide Layer Characterization

As was discussed above the main feature which increases the ignition temperature of magnesium alloys is the creation of the oxide film. This film in the case of WE43 alloy consists of various oxides which are shown on the cuts after exposition to 800 °C in Figure 8. The film contained Y, Gd, Nd, Mg, Dy, Zr, and even Er although the total amount of Er in the alloy is very low. However, according to the X-ray diffraction (Figure 9), there is only a low amount of MgO and Y_2O_3, which is isomorphous with other RE oxides. On the other hand, ZrO_2 is not isomorphous and it was not detected by XRD even though according to the EDS there is Zr in the oxide layer. This phenomenon can be associated with the solubility of specified elements in Y_2O_3 oxide. One of the oxides may be $YZrO_3$, which is isomorphous with Y_2O_3. The cell parameter of the measured oxide layer was approximately 10.624 Å which is a slightly higher value compared to Y_2O_3 characterized by 10.604 Å (Table 6). This is due to the substitution of Y for another REs and/or Zr, where only Zr and Er are smaller, and therefore, reduces the cell parameter.
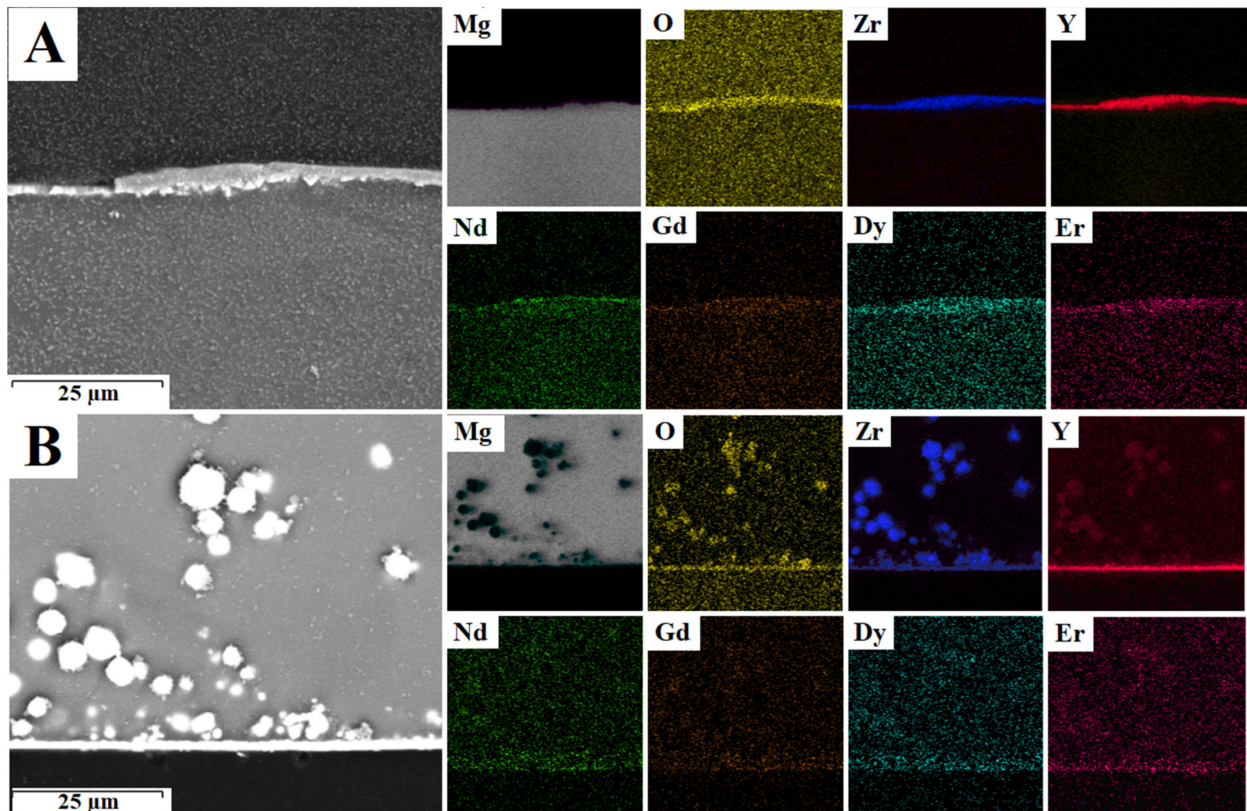
Figure 8. EDS analysis of the cut of the WE43 alloy (AC) after exposure to 800 °C, (**A**) top, (**B**) bottom.
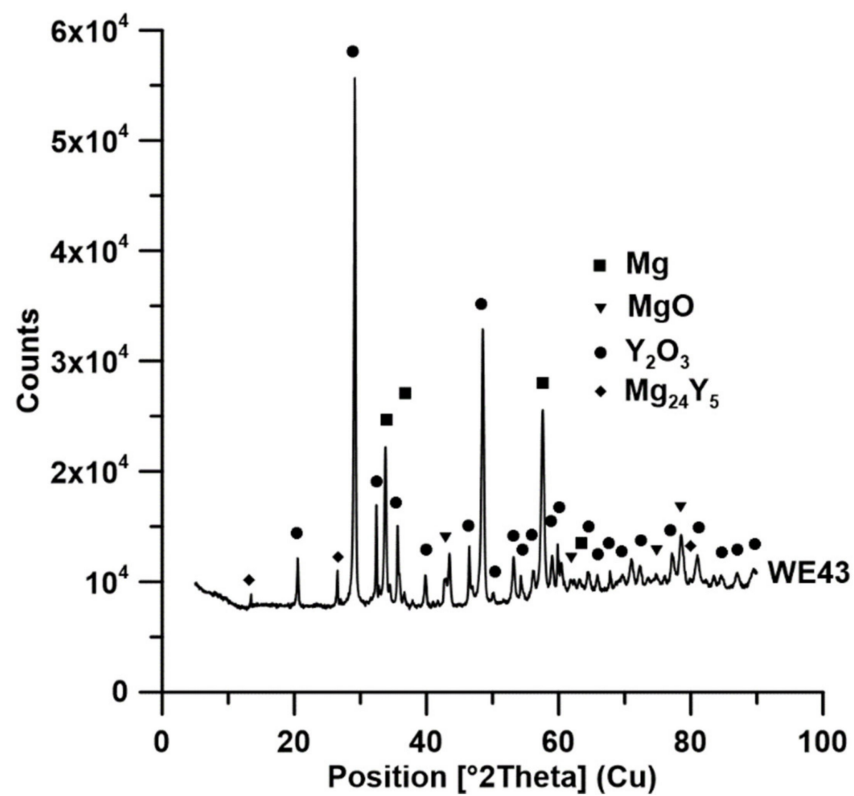

**Figure 9.** XRD diffraction of oxides on the surface of material exposed to 800 °C (AC).

Table 6. Composition of the oxide layer and cell parameters of individual oxides [61–66].

Element	Y	Nd	Gd	Dy	Er	Zr
EDS (wt %)	57.5 ± 3.2	4.2 ± 0.2	1.1 ± 0.1	1.4 ± 0.1	1.0 ± 0.1	1.8 ± 0.2
Cell parameter of oxide (Å)	10.604	11.102	10.722	10.672	10.547	10.515

We observed a slight difference between the top and bottom of the sample exposed to the increased temperature. The top layer (Figure 8A) was slightly thicker and uneven which is probably associated with the shape of the material after melting. The bottom layer was straight as it laid down on the surface of the crucible. However, there were quite large (1–10 μm) round-shaped particles of $YZrO_3$. The presence of these particles on the bottom of the sample is probably caused by the gravitational separation in a molten state.

Compared to the pure Mg exposed to 650 °C there is up to 50 μm thick porous layer of MgO [58]. This layer has no protective effect as oxygen can penetrate this layer and incorporate into the Mg matrix [13].

The creation of oxides should proceed according to the thermodynamic relations. Therefore, the standard Gibbs energy of formation of oxides (ΔGf0) (Figure 10) reveals the affinity of selected elements to oxygen—the lower the curve representing oxidation reaction in this diagram is, the greater the affinity to oxygen. It is evident, that thermodynamically the most stable oxide is Y_2O_3, which is in accordance with the findings acquired by EDS or X-ray diffraction. Other alloying elements are involved in the oxide layer due to the dissolution in Y_2O_3. As has been already suggested, this improves the mechanical properties of this oxide layer. The ignition temperature above the melting point of magnesium is highly dependent on the integrity of the oxide layer which holds the melt inside and slows down the diffusion of Mg to the surface. Thus, improvement of mechanical properties of Y_2O_3 due to the substitution of other elements results in a high ignition temperature.
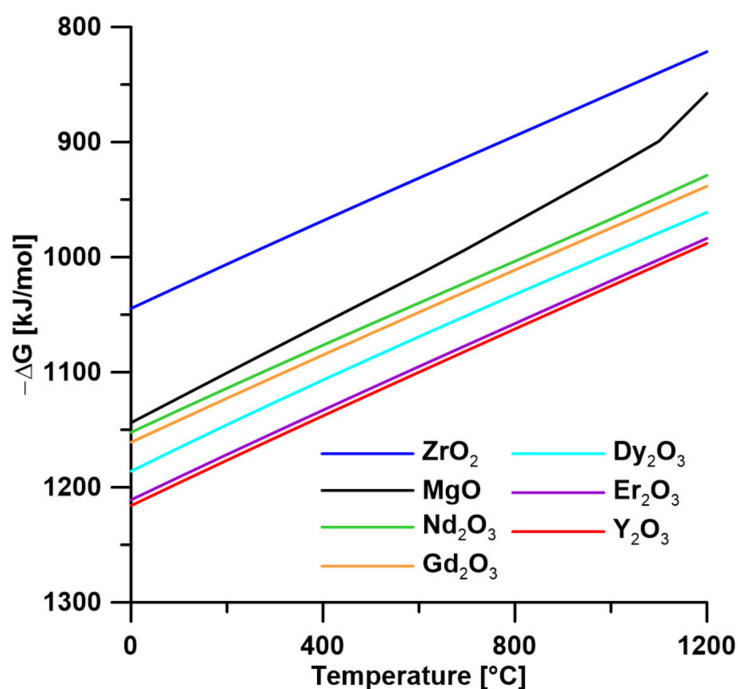
Figure 10. Calculated ΔGf0 for the presented oxides for 1 mol O_2 at a standard pressure of 101 kPa.

4. Conclusions

One of the most advanced commercial magnesium alloys WE43 was prepared by various processing techniques including casting, heat treatment, extrusion, and SPS. The obtained TYS and UTS values ranged from 140 to 280 MPa and 210 to 325 MPa, respectively.

The dominant effect was attributed to the average grain size and distribution of intermetallic phases in the microstructure. The latter one also significantly affected corrosion behavior. Dissolution of intermetallic phases in the microstructure increased the content of alloying elements in the solid solution, helping to form more protective oxide layers during degradation. Contrary, coarse intermetallic phases and inhomogeneous microstructures led to a localized degradation and high corrosion rates. The ignition temperature of all prepared samples was above 850 °C, which is suitable for application in the aviation industry. Nevertheless, the concentration of alloying elements in the solid solution, homogeneity of microstructure, and concentration of intermetallic phases significantly affected the ignition temperature. The high content of alloying elements in the solid solution and the presence of thermally stable intermetallic phases instead of a low-melting eutectic mixture are the most appropriate for the increase of ignition resistance. The protective effect of Y_2O_3 doped by other alloying elements substituting Y in the lattice is the main reason behind the high ignition temperature of WE43 alloy.

Conflicts of Interest: The authors declare no conflict of interest.

References

1. Liu, C.; Lu, S.; Fu, Y.; Zhang, H. Flammability and the oxidation kinetics of the magnesium alloys AZ31, WE43, and ZE10. *Corros. Sci.* **2015**, *100*, 177–185. [CrossRef]
2. Mondet, M.; Barraud, E.; Lemonnier, S.; Guyon, J.; Allain, N.; Grosdidier, T. Microstructure and mechanical properties of AZ91 magnesium alloy developed by Spark Plasma Sintering. *Acta Mater.* **2016**, *119*, 55–67. [CrossRef]
3. Tekumalla, S.; Si Chun, L.; Gupta, M. Preprocessing of powder to enhance mechanical and thermal response of bulk magnesium. *Metal Powder Rep.* **2019**, *74*, 137–140. [CrossRef]
4. Tekumalla, S.; Gupta, M. An insight into ignition factors and mechanisms of magnesium based materials: A review. *Mater. Des.* **2017**, *113*, 84–98. [CrossRef]
5. Czerwinski, F. Controlling the ignition and flammability of magnesium for aerospace applications. *Corros. Sci.* **2014**, *86*, 1–16. [CrossRef]
6. Zhou, N.; Zhang, Z.; Dong, J.; Jin, L.; Ding, W. Selective oxidation behavior of an ignition-proof Mg-Y-Ca-Ce alloy. *J. Rare Earth* **2013**, *31*, 1003–1008. [CrossRef]
7. Pan, F.; Yang, M.; Chen, X. A Review on Casting Magnesium Alloys: Modification of Commercial Alloys and Development of New Alloys. *J. Mater. Sci. Technol.* **2016**, *32*, 1211–1221. [CrossRef]
8. Aydin, D.S.; Bayindir, Z.; Hoseini, M.; Pekguleryuz, M.O. The high temperature oxidation and ignition behavior of Mg–Nd alloys part I: The oxidation of dilute alloys. *J. Alloys Compd.* **2013**, *569*, 35–44. [CrossRef]
9. Yu, X.; Shen, S.; Jiang, B.; Jiang, Z.; Yang, H.; Pan, F. The effect of the existing state of Y on high temperature oxidation properties of magnesium alloys. *Appl. Surf. Sci.* **2016**, *370*, 357–363. [CrossRef]
10. Ning, Z.L.; Zhao, X.Y.; Luo, A.A.; Liu, H.H.; Liang, W.Z.; Huang, Y.J.; Cao, F.Y.; Sun, J.F. The melt protection mechanism of an SO2/CO2 gas mixture for a magnesium-rare-earth based alloy. *J. Alloys Compd.* **2017**, *722*, 101–107. [CrossRef]
11. Fan, J.; Chen, Z.; Yang, W.; Fang, S.; Xu, B. Effect of yttrium, calcium and zirconium on ignition-proof principle and mechanical properties of magnesium alloys. *J. Rare Earths* **2012**, *30*, 74–78. [CrossRef]

12. Go, Y.; Jo, S.M.; Park, S.H.; Kim, H.S.; You, B.S.; Kim, Y.M. Microstructure and mechanical properties of non-flammable Mg-8Al-0.3Zn-0.1Mn-0.3Ca-0.2Y alloy subjected to low-temperature, low-speed extrusion. *J. Alloys Compd.* **2018**, *739*, 69–76. [CrossRef]

13. Kim, Y.M.; Yim, C.D.; Kim, H.S.; You, B.S. Key factor influencing the ignition resistance of magnesium alloys at elevated temperatures. *Scr. Mater.* **2011**, *65*, 958–961. [CrossRef]

14. Chen, Z.-H.; Ren, X.-P.; Zhang, Y. Effect of RE on the ignition-proof, microstructure and properties of AZ91D magnesium alloy. *Int. J. Miner. Metall. Mater.* **2005**, *12*, 540–544.

15. Prasad, A.; Shi, Z.; Atrens, A. Influence of Al and Y on the ignition and flammability of Mg alloys. *Corros. Sci.* **2012**, *55*, 153–163. [CrossRef]

16. Han, G.; Chen, D.; Chen, G.; Huang, J. Development of non-flammable high strength extruded Mg-Al-Ca-Mn alloys with high Ca/Al ratio. *J. Mater. Sci. Technol.* **2018**, *34*, 2063–2068. [CrossRef]

17. Liu, M.; Shih, D.S.; Parish, C.; Atrens, A. The ignition temperature of Mg alloys WE43, AZ31 and AZ91. *Corros. Sci.* **2012**, *54*, 139–142. [CrossRef]

18. Ravi Kumar, N.V.; Blandin, J.J.; Suéry, M.; Grosjean, E. Effect of alloying elements on the ignition resistance of magnesium alloys. *Scr. Mater.* **2003**, *49*, 225–230. [CrossRef]

19. Eyring, H.; Zwolinski, B. The critical temperature for combustion of metals and their alloys. In *Record of Chemical Progress (Wayne State University Press)*; Wayne University: Detroit, MI, USA, 1947.

20. Bungaro, C.; Noguera, C.; Ballone, P.; Kress, W. Early oxidation stages of Mg (0001): A density functional study. *Phys. Rev. Lett.* **1997**, *79*, 4433. [CrossRef]

21. Schröder, E. Interaction effects in magnesium oxidation: A lattice-gas simulation. *Comput. Mater. Sci.* **2002**, *24*, 105–110. [CrossRef]

22. Kubásek, J.; Dvorský, D.; Čavojský, M.; Vojtěch, D.; Beronská, N.; Fousová, M. Superior Properties of Mg–4Y–3RE–Zr Alloy Prepared by Powder Metallurgy. *J. Mater. Sci. Technol.* **2017**, *33*, 652–660. [CrossRef]

23. Nie, J.F.; Muddle, B.C. Characterisation of strengthening precipitate phases in a Mg–Y–Nd alloy. *Acta Mater.* **2000**, *48*, 1691–1703. [CrossRef]

24. Jiang, H.S.; Zheng, M.Y.; Qiao, X.G.; Wu, K.; Peng, Q.Y.; Yang, S.H.; Yuan, Y.H.; Luo, J.H. Microstructure and mechanical properties of WE43 magnesium alloy fabricated by direct-chill casting. *Mater. Sci. Eng. A* **2017**, *684*, 158–164. [CrossRef]

25. Xiang, C.; Gupta, N.; Coelho, P.; Cho, K. Effect of microstructure on tensile and compressive behavior of WE43 alloy in as cast and heat treated conditions. *Mater. Sci. Eng. A* **2018**, *710*, 74–85. [CrossRef]

26. Bütev Öcal, E.; Esen, Z.; Aydınol, K.; Dericioğlu, A.F. Comparison of the short and long-term degradation behaviors of as-cast pure Mg, AZ91 and WE43 alloys. *Mater. Chem. Phys.* **2020**, *241*, 122350. [CrossRef]

27. Yang, C.; Gupta, N.; Ding, H.; Xiang, C. Effect of Microstructure on Corrosion Behavior of WE43 Magnesium Alloy in As Cast and Heat-Treated Conditions. *Metals* **2020**, *10*, 1552. [CrossRef]

28. Dvorsky, D.; Kubasek, J.; Jablonska, E.; Lipov, J.; Vojtech, D. High strength AM50 magnesium alloy as a material for possible stent application in medicine. *Mater. Technol.* **2019**, *34*, 838–842. [CrossRef]

29. Asmussen, R.M.; Jakupi, P.; Danaie, M.; Botton, G.A.; Shoesmith, D.W. Tracking the corrosion of magnesium sand cast AM50 alloy in chloride environments. *Corros. Sci.* **2013**, *75*, 114–122. [CrossRef]

30. Gao, G.-J.; Zeng, M.-Q.; Zhang, E.-L.; Zeng, R.-C.; Cui, L.-Y.; Xu, D.-k.; Wang, F.-Q.; Kannan, M.B. Dealloying corrosion of anodic and nanometric Mg41Nd5 in solid solution-treated Mg-3Nd-1Li-0.2Zn alloy. *J. Mater. Sci. Technol.* **2021**, *83*, 161–178. [CrossRef]

31. Zhang, J.; Jiang, B.; Yang, Q.; Huang, D.; Tang, A.; Pan, F.; Han, Q. Role of second phases on the corrosion resistance of Mg-Nd-Zr alloys. *J. Alloys Compd.* **2020**, *849*, 156619. [CrossRef]

32. Dvorsky, D.; Kubasek, J.; Jablonska, E.; Kaufmanova, J.; Vojtech, D. Mechanical, corrosion and biological properties of advanced biodegradable Mg-MgF2 and WE43-MgF2 composite materials prepared by spark plasma sintering. *J. Alloys Compd.* **2020**, *825*, 154016. [CrossRef]

33. Minárik, P.; Zemková, M.; Lukáč, F.; Bohlen, J.; Knapek, M.; Král, R. Microstructure of the novel biomedical Mg–4Y–3Nd alloy prepared by spark plasma sintering. *J. Alloys Compd.* **2020**, *819*, 153008. [CrossRef]

34. Kang, Y.; Huang, Z.; Zhao, H.; Gan, C.; Zhou, N.; Zheng, K.; Zhang, J.; Pan, F.; Huang, J.C.; Wang, S. Comparative Study of Hot Deformation Behavior and Microstructure Evolution of As-Cast and Extruded WE43 Magnesium Alloy. *Metals* **2020**, *10*, 429. [CrossRef]

35. Kiełbus, A.; Rzychoń, T.; Lityńska-Dobrzyńska, L.; Dercz, G. Characterization of β and Mg41Nd5 Equilibrium Phases in Elektron 21 Magnesium Alloy after Long-Term Annealing. *Solid State Phenom.* **2010**, *163*, 106–109. [CrossRef]

36. Dvorský, D.; Kubásek, J.; Průša, F.; Kristianová, E.; Vojtěch, D. Specific interface prepared by the SPS of chemically treated Mg-based powder. *Mater. Chem. Phys.* **2021**, *261*. [CrossRef]

37. Dvorský, D.; Kubásek, J.; Roudnická, M.; Průša, F.; Nečas, D.; Minárik, P.; Stráská, J.; Vojtěch, D. The effect of powder size on the mechanical and corrosion properties and the ignition temperature of WE43 alloy prepared by spark plasma sintering. *J. Magnes. Alloys* **2021**. [CrossRef]

38. Zemkova, M.; Minarik, P.; Knapek, M.; Sasek, S.; Dittrich, J.; Kral, R. Microstructure and Mechanical Strength of Attritor-Milled and Spark Plasma Sintered Mg-4Y-3Nd Alloy. *Crystals* **2020**, *10*, 574. [CrossRef]

39. Minarik, P.; Zemkova, M.; Knapek, M.; Sasek, S.; Dittrich, J.; Lukac, F.; Kozlik, J.; Kral, R. Effect of Short Attritor-Milling of Magnesium Alloy Powder Prior to Spark Plasma Sintering. *Materials* **2020**, *13*, 3973. [CrossRef]

40. Kubásek, J.; Dvorský, D.; Čavojský, M.; Roudnická, M.; Vojtěch, D. WE43 magnesium alloy—Material for challenging applications. *Kov. Mater.* **2019**, *57*, 159–165. [CrossRef]

41. Barnett, M.R.; Sullivan, A.; Stanford, N.; Ross, N.; Beer, A. Texture selection mechanisms in uniaxially extruded magnesium alloys. *Scr. Mater.* **2010**, *63*, 721–724. [CrossRef]

42. Kleiner, S.; Uggowitzer, P.J. Mechanical anisotropy of extruded Mg–6% Al–1% Zn alloy. *Mater. Sci. Eng. A* **2004**, *379*, 258–263. [CrossRef]

43. Stanford, N.; Barnett, M.R. The origin of "rare earth" texture development in extruded Mg-based alloys and its effect on tensile ductility. *Mater. Sci. Eng. A* **2008**, *496*, 399–408. [CrossRef]

44. Dvorský, D.; Kubásek, J.; Voňavková, I.; Vojtěch, D. Structure, mechanical and corrosion properties of extruded Mg-Nd-Zn, Mg-Y-Zn and Mg-Y-Nd alloys. *Mater. Sci. Technol.* **2019**, *35*, 520–529. [CrossRef]

45. Kubásek, J.; Dvorský, D.; Veselý, J.; Minárik, P.; Zemková, M.; Vojtěch, D. Characterization of the High-Strength Mg–3Nd–0.5Zn Alloy Prepared by Thermomechanical Processing. *Acta Metall. Sin.* **2019**, *32*, 321–331. [CrossRef]

46. Yu, H.; Xin, Y.; Wang, M.; Liu, Q. Hall-Petch relationship in Mg alloys: A review. *J. Mater. Sci. Technol.* **2018**, *34*, 248–256. [CrossRef]

47. Kang, Y.H.; Wu, D.; Chen, R.S.; Han, E.H. Microstructures and mechanical properties of the age hardened Mg–4.2Y–2.5Nd–1Gd–0.6Zr (WE43) microalloyed with Zn. *J. Magnes. Alloys* **2014**, *2*, 109–115. [CrossRef]

48. Kniffka, W.; Eichmann, M.; Witt, G.; Gieseke, M.; Tandon, R.; Kiesow, T.; Wessarges, Y.; Nölke, C.; Kaierle, S. Selektives Laserstrahlschmelzen von Elektron® MAP 43 Magnesiumpulver/Selective Laser Melting of Elektron® MAP 43 Magnesium Powder. In *Rapid.Tech—International Trade Show & Conference for Additive Manufacturing*; Carl Hanser Verlag GmbH & Co. KG: Munich, Germany, 2016; pp. 244–252.

49. Zhang, X.; Yuan, G.; Mao, L.; Niu, J.; Ding, W. Biocorrosion properties of as-extruded Mg–Nd–Zn–Zr alloy compared with commercial AZ31 and WE43 alloys. *Mater. Lett.* **2012**, *66*, 209–211. [CrossRef]

50. Asqardoust, S.; Zarei Hanzaki, A.; Abedi, H.R.; Krajnak, T.; Minárik, P. Enhancing the strength and ductility in accumulative back extruded WE43 magnesium alloy through achieving bimodal grain size distribution and texture weakening. *Mater. Sci. Eng. A* **2017**, *698*, 218–229. [CrossRef]

51. Xu, X.; Chen, X.; Du, W.; Geng, Y.; Pan, F. Effect of Nd on microstructure and mechanical properties of as-extruded Mg-Y-Zr-Nd alloy. *J. Mater. Sci. Technol.* **2017**, *33*, 926–934. [CrossRef]

52. Zumdick, N.A.; Jauer, L.; Kersting, L.C.; Kutz, T.N.; Schleifenbaum, J.H.; Zander, D. Additive manufactured WE43 magnesium: A comparative study of the microstructure and mechanical properties with those of powder extruded and as-cast WE43. *Mater. Charact.* **2019**, *147*, 384–397. [CrossRef]

53. Liu, M.; Schmutz, P.; Uggowitzer, P.J.; Song, G.; Atrens, A. The influence of yttrium (Y) on the corrosion of Mg–Y binary alloys. *Corros. Sci.* **2010**, *52*, 3687–3701. [CrossRef]

54. Birbilis, N.; Zhang, M.X.; Estrin, Y. Surface Grain Size Effects on the Corrosion of Magnesium. *Key Eng. Mater.* **2008**, *384*, 229–240. [CrossRef]

55. Li, N.; Guo, C.; Wu, Y.H.; Zheng, Y.F.; Ruan, L.Q. Comparative study on corrossion behaviour of pure Mg and WE43 alloy in static, stirring and flowing Hank´s solution. *Corros. Eng. Sci. Technol.* **2012**, *47*, 346–351. [CrossRef]

56. Argade, G.R.; Panigrahi, S.K.; Mishra, R.S. Effects of grain size on the corrosion resistance of wrought magnesium alloys containing neodymium. *Corros. Sci.* **2012**, *58*, 145–151. [CrossRef]

57. Han, D.; Zhang, J.; Huang, J.; Lian, Y.; He, G. A review on ignition mechanisms and characteristics of magnesium alloys. *J. Magnes. Alloys* **2020**, *8*, 329–344. [CrossRef]

58. Dvorsky, D.; Kubasek, J.; Vojtech, D.; Minarik, P. Novel aircraft Mg-Y-Gd-Ca alloys with high ignition temperature and suppressed flammability. *Mater. Lett.* **2020**, *264*, 127313. [CrossRef]

59. Dvorsky, D.; Dalibor Vojtech, J.K.; Vojtech, D.; Minárik, P.; Straska, J. The effect of Y, Gd and Ca on the ignition temperature of extruded magnesium alloys. *Mater.Technol.* **2020**, *54*, 669–675. [CrossRef]

60. Fan, J.; Yang, C.; Xu, B. Effect of Ca and Y additions on oxidation behavior of magnesium alloys at high temperatures. *J. Rare Earths* **2012**, *30*, 497–502. [CrossRef]

61. Ferreira, F.F.; Granado, E.; Carvalho, W., Jr.; Kycia, S.W.; Bruno, D.; Droppa, R., Jr. X-ray powder diffraction beamline at D10B of LNLS: Application to the Ba2FeReO6 double perovskite. *J. Synchrotron Radiat.* **2006**, *13*, 46–53. [CrossRef] [PubMed]

62. Artini, C.; Pani, M.; Plaisier, J.R.; Costa, G.A. Structural study of Nd oxidation by means of in-situ synchrotron X-ray diffraction (400 ≤ T ≤ 700 °C). *Solid State Ion.* **2014**, *257*, 38–41. [CrossRef]

63. Pires, A.M.; Davolos, M.R.; Paiva-Santos, C.O.; Stucchi, E.B.; Flor, J. New X-ray powder diffraction data and Rietveld refinement for Gd2O3 monodispersed fine spherical particles. *J. Solid State Chem.* **2003**, *171*, 420–423. [CrossRef]

64. Chandrasekhar, M.; Nagabhushana, H.; Sudheerkumar, K.H.; Dhananjaya, N.; Sharma, S.C.; Kavyashree, D.; Shivakumara, C.; Nagabhushana, B.M. Comparison of structural and luminescence properties of Dy2O3 nanopowders synthesized by co-precipitation and green combustion routes. *Mater. Res. Bull.* **2014**, *55*, 237–245. [CrossRef]

65. Moon, R.M.; Koehler, W.C.; Child, H.R.; Raubenheimer, L.J. Magnetic structures of Er2O3 and Yb2O3. *Phys. Rev.* **1968**, *176*, 722–731. [CrossRef]

66. Baldinozzi, G.; Bérar, J.F.; Calvarin-Amiri, G. Rietveld Refinement of Two-Phase Zr-Doped Y2O3. *Mater. Sci. Forum* **1998**, *278–281*, 680–685. [CrossRef]